

Hybrid simplified spherical harmonics with diffusion equation for light propagation in tissues

This content has been downloaded from IOPscience. Please scroll down to see the full text.

2015 Phys. Med. Biol. 60 6305

(<http://iopscience.iop.org/0031-9155/60/16/6305>)

View [the table of contents for this issue](#), or go to the [journal homepage](#) for more

Download details:

This content was downloaded by: charles_chen

IP Address: 128.211.253.140

This content was downloaded on 04/08/2015 at 01:39

Please note that [terms and conditions apply](#).

Hybrid simplified spherical harmonics with diffusion equation for light propagation in tissues

Xueli Chen¹, Fangfang Sun¹, Defu Yang¹, Shenghan Ren¹,
Qian Zhang² and Jimin Liang¹

¹ Engineering Research Center of Molecular and Neuro Imaging of Ministry of Education and School of Life Science and Technology, Xidian University, Xi'an, Shaanxi 710071, People's Republic of China

² Institute of Automation, Chinese Academy of Sciences, Beijing 100190, People's Republic of China

E-mail: xlchen@xidian.edu.cn and jimleung@mail.xidian.edu.cn

Received 1 March 2015, revised 26 May 2015

Accepted for publication 2 June 2015

Published 3 August 2015



Abstract

Aiming at the limitations of the simplified spherical harmonics approximation (SP_N) and diffusion equation (DE) in describing the light propagation in tissues, a hybrid simplified spherical harmonics with diffusion equation (HSDE) based diffuse light transport model is proposed. In the HSDE model, the living body is first segmented into several major organs, and then the organs are divided into high scattering tissues and other tissues. DE and SP_N are employed to describe the light propagation in these two kinds of tissues respectively, which are finally coupled using the established boundary coupling condition. The HSDE model makes full use of the advantages of SP_N and DE, and abandons their disadvantages, so that it can provide a perfect balance between accuracy and computation time. Using the finite element method, the HSDE is solved for light flux density map on body surface. The accuracy and efficiency of the HSDE are validated with both regular geometries and digital mouse model based simulations. Corresponding results reveal that a comparable accuracy and much less computation time are achieved compared with the SP_N model as well as a much better accuracy compared with the DE one.

Keywords: hybrid light transport model, SP_N , DE, HSDE, fluorescence/bioluminescence tomography

(Some figures may appear in colour only in the online journal)

1. Introduction

Fluorescence tomography (FMT), as an emerging and promising imaging technique, has become an attractive tool for biological and biomedical research (Ntziachristos *et al* 2002a, 2002b, Ntziachristos *et al* 2005, Zacharakis *et al* 2005, Ale *et al* 2012). With the goal of providing three-dimensional (3D) images, FMT can accurately detect 3D distribution and concentration of fluorescent probes inside a living body using the boundary measurements from a non-contact detector (Hyde *et al* 2010, Li *et al* 2012, Darne *et al* 2014). Thus, more and more applications have been achieved for this technique in recent years because of its high sensitivity, noninvasiveness, 3D *in vivo* imaging, and possibility of revealing functional information with fluorescent probes, including tumor imaging (Fortin *et al* 2012, Erickson *et al* 2013, Lu *et al* 2013, Zhang *et al* 2013, 2014), tumor treatment and pharmacokinetic analysis (Ntziachristos *et al* 2002a, 2002b, Stuker *et al* 2011, Liu *et al* 2012a, Davisa *et al* 2013, Zhang *et al* 2014), arthrosis and bone imaging (Lambers *et al* 2012, Mohajerani *et al* 2014), atherosclerosis (Nahrendorf *et al* 2009), and Alzheimer's disease imaging (Hyde *et al* 2009).

Establishing an accurate and rapid forward model which properly characterizes the fluorescence propagation in tissues is crucial for FMT reconstruction that provides the location of the fluorophore, the distribution of the fluorescence quantum yield, and the images of fluorescent lifetime. Because the diffusion equation (DE) is easy to be solved with high accuracy in a diffuse medium, it has been initially employed in FMT reconstruction (Ntziachristos *et al* 2002a, 2002b, Soubret *et al* 2005, Joshi *et al* 2006, Wang *et al* 2007, 2009, Tan and Jiang 2008, Freiburger *et al* 2010, Gao *et al* 2010, Hyde *et al* 2010, Rudge *et al* 2010, Zhu *et al* 2011, Ale *et al* 2012, Li *et al* 2012, Liu *et al* 2012b, Yi *et al* 2013, Wu and Gayen 2014). Although DE provides high efficiency for describing fluorescence propagation in tissues and is popular in FMT, it becomes inaccurate in some cases, such as in domains near the source, with high or too low absorption, with low scattering, and small-sized tissues, which are pertinent in whole-body small animal imaging (Gibson *et al* 2005). To conquer the limitations of DE, the radiative transfer equation (RTE) and Monte Carlo (MC) based reconstruction methods were also developed recently (Joshi *et al* 2008, Kim *et al* 2010, Quan *et al* 2011, Chen *et al* 2012). RTE and MC are regarded as the golden standard methods for describing the light propagation in a turbid medium, which would provide an accurate forward solver for FMT reconstruction. However, a huge computational burden and time cost hinder the practical applications of RTE and MC based reconstruction methods. The simplified spherical harmonics (SP_N) approximation has also been employed as the forward model for FMT (Han *et al* 2010, Klose and Pöschinger 2011), with the purpose of reducing the computational cost of the RTE or MC based one. As a higher order approximation to RTE, SP_N inherits its high accuracy, but the computational cost is still large compared with the DE model. In summary, the DE based forward model has high computational efficiency, but is only valid in a highly diffuse medium (high scattering tissues); the SP_N , RTE, and MC based forward models provide adequate accuracy in various types of tissues, such as high and low scattering as well as high absorption ones, but bring about a large computational burden and time cost. In the living body, diverse organs have different optical properties, which might be sorted into different types of tissues using the predefined parameter to differentiate the optical behavior of various organs (Yang *et al* 2015). Taking the whole-body small animal imaging as an example, the low scattering liver and lungs are surrounded by high scattering adipose, kidneys, heart, etc. Thus, developing a new forward model, which is not only accurate but also efficient for the living body consisting of different types of tissues, is becoming much more important for further extension of the applications of FMT in biological and biomedical research. Some hybrid light transport

models have been developed in the past decades (Firbank *et al* 1996, Dehghani *et al* 1999, Tarvainen 2005, Gorpas *et al* 2010, Gorpas *et al* 2012, Lehtikangas *et al* 2013). However, they are either limited by using RTE (Tarvainen 2005, Gorpas *et al* 2010, 2012, Lehtikangas *et al* 2013) or proposed for the problem of light propagation in void regions (Firbank *et al* 1996, Dehghani *et al* 1999). In our previous study (Yang *et al* 2013), the hybrid SP_N with radiosity model (HSRM) was proposed to describe light propagation in the turbid media with high, low scattering and high absorption as well as void region, but it still suffers the large computational burden and time cost of SP_N .

In this study, the hybrid simplified spherical harmonics with diffusion equation (HSDE) is proposed as the forward model for fluorescent light propagation in tissues. In the HSDE based model, the tissues are first classified into two categories, the high scattering tissues and other tissues, using a defined sorting criterion which integrates the commonly used criterion and our newly investigated results (Dehghani *et al* 1999, Yang *et al* 2015). DE and SP_N are then used to describe light propagation in high scattering and other tissues respectively. By establishing a boundary coupling condition which depicts the transformation of physical quantities at the boundary of different equations, the unified form of HSDE can be finally obtained, which takes both the high-precision advantage of SP_N and the low-computation-cost advantage of DE into account and provides a perfect balance between accuracy and computation time. With the help of the finite element method, the HSDE is solved for light flux density map on body surface. In the following sections, the performance of HSDE model is verified and evaluated with a series of simulations from the regular shape to digital mouse based geometries.

2. Methods

2.1. Construction of the HSDE model

Prior to the construction of the forward model of fluorescent light propagation, the biological tissues should be specifically sorted as follows. First of all, the living body can be segmented into several major organs based on *a priori* information of anatomic structure. Then, the major organs are classified into different categories using the predefined sorting criterion. The classification procedure obeys the following expression:

$$\Omega = \begin{cases} \Omega_h & \mu'_s/\mu_a \geq \zeta \\ \Omega_l & \mu'_s/\mu_a < \zeta \text{ or } \mu_a \geq \chi, \end{cases} \quad (1)$$

where Ω denotes the domain of the living body; Ω_h is that of the category of high scattering regions; Ω_l is of the category of the other regions, including low scattering and high absorption tissues; μ_a is the absorption coefficient; μ'_s is the reduced scattering coefficient that can be calculated by $\mu'_s = \mu_s(1 - g)$, where g is the anisotropy factor; ζ and χ are parameters for tissue classification. Based on the commonly used criterion and our newly investigated results (Dehghani *et al* 1999, Yang *et al* 2015), ζ and χ are set to be 10 mm^{-1} and 0.2 mm^{-1} in this study, respectively.

After the tissues are specifically classified, DE and SP_N are then utilized to describe light propagation in high scattering and other regions respectively. Previous studies have illustrated that the third order SP_N (SP_3) can yield an adequate accuracy with an acceptable computational burden (Lu *et al* 2009, Liu *et al* 2010), so that it was actually selected as a case of SP_N here. The concrete form of SP_3 as well as the relevant boundary condition can be detailed as (Klose and Larsen 2006, Lu *et al* 2009, Liu *et al* 2010):

$$\begin{cases} -\nabla \cdot \frac{1}{3\mu_{a1}(r)} \nabla \Phi_1(r) + \mu_a(r)\Phi_1(r) - \\ \frac{2}{3}\mu_a(r)\Phi_2(r) = S(r) \\ -\nabla \cdot \frac{1}{7\mu_{a3}(r)} \nabla \Phi_2(r) - \frac{2}{3}\mu_a(r)\Phi_1(r) + \\ \left(\frac{4}{9}\mu_a(r) + \frac{5}{9}\mu_{a2}(r)\right)\Phi_2(r) = -\frac{2}{3}S(r) \end{cases} \quad r \in \Omega_i, \quad (2a)$$

$$\begin{cases} \frac{1+B_1}{3\mu_{a1}(r)} v \cdot \nabla \Phi_1(r) - \frac{D_1}{\mu_{a3}(r)} v \cdot \nabla \Phi_2(r) = \\ -\left(\frac{1}{2} + A_1\right)\Phi_1(r) + \left(\frac{1}{8} + C_1\right)\Phi_2(r) \\ -\frac{D_2}{\mu_{a1}(r)} v \cdot \nabla \Phi_1(r) + \frac{1+B_2}{7\mu_{a3}(r)} v \cdot \nabla \Phi_2(r) = \\ \left(\frac{1}{8} + C_2\right)\Phi_1(r) - \left(\frac{7}{24} + A_2\right)\Phi_2(r) \end{cases} \quad r \in \partial\Omega_i, \quad (2b)$$

where $\partial\Omega_i$ denotes the boundary of the other regions Ω_i ; $\Phi_k(r)$ ($k = 1, 2$) are the composite moments relevant to the nodal flux density; $S(r)$ is the light source; $\mu_{ai}(r)$ ($i = 1, 2, 3$) and $\mu_a(r)$ are absorption related parameters; A_k, B_k, C_k, D_k ($k = 1, 2$) are boundary related parameters; and v is the unit direction vector toward the body surface. The parameters are detailed in (Klose and Larsen 2006, Lu *et al* 2009). The exiting partial current J at the outer boundary of the other regions can be expressed as follows (Klose and Larsen 2006, Lu *et al* 2009, Liu *et al* 2010):

$$J_{SP3}(r) = \beta_1(r)\Phi_1(r) + \beta_2(r)\Phi_2(r) \quad r \in \partial\Omega_i, \quad (3)$$

where $\beta_k(r)$ ($k = 1, 2$) can be referenced from (Liu *et al* 2010).

From previous studies (Soubret *et al* 2005, Joshi *et al* 2006, Wang *et al* 2007, 2009, Tan and Jiang 2008, Freiburger *et al* 2010, Gao *et al* 2010, Rudge *et al* 2010, Zhu *et al* 2011, Liu *et al* 2012b, Yi *et al* 2013, Wu and Gayen 2014), a conclusion can be obtained that DE can be used to accurately and efficiently describe light propagation in the high scattering regions. DE and its Robin boundary condition can be detailed as (Arridge 1999):

$$-\nabla \cdot (D(r) \nabla \Phi_0(r)) + \mu_a(r)\Phi_0(r) = S(r) \quad r \in \Omega_h, \quad (4a)$$

$$\Phi_0(r) + \frac{1}{\beta_0(r)} D(r) (v \cdot \nabla \Phi_0(r)) = 0 \quad r \in \partial\Omega_h, \quad (4b)$$

where $\partial\Omega_h$ shows the boundary of high scattering regions Ω_h ; $\Phi_0(r)$ is the nodal flux density; $D(r) = (3(\mu_a(r) + \mu'_s(r)))^{-1}$ is the diffuse coefficient; and $\beta_0(r)$ is a parameter relevant to the mismatched refractive indices. In the same way, the exiting partial current J at the outer boundary of high scattering regions can be expressed as (Cong *et al* 2005):

$$J_{DE}(r) = \beta_0(r)\Phi_0(r) \quad r \in \partial\Omega_h. \quad (5)$$

To integrate SP₃ and DE, a boundary coupling condition at the interface of the other and high scattering regions is established according to the law of conservation of flux (Ripoll and Nieto-Vesperinas 1999a, 1999b) and can be defined as:

$$J_{SP3}(r) = J_{DE}(r) \quad r \in B, \quad (6)$$

where B represents the shared boundary between the other and high scattering regions and is defined as the intersection between $\partial\Omega_l$ and $\partial\Omega_h$. Substituting equations (3) and (5) into equation (6), the following relationship can be addressed:

$$\Phi_0(r) = \frac{\beta_1(r)}{\beta_0(r)}\Phi_1(r) + \frac{\beta_2(r)}{\beta_0(r)}\Phi_2(r). \quad (7)$$

By introducing an indicator factor that indicates the category of biological tissues and incorporating the predefined boundary coupling condition simultaneously, the unified form of HSDE can be obtained:

$$\left\{ \begin{array}{l} (1 - \sigma(r)) \left\{ -\nabla \cdot \frac{1}{3\mu_{a1}(r)} \nabla \Phi_1(r) + \mu_a(r)\Phi_1(r) - \frac{2}{3}\mu_a(r)\Phi_2(r) \right\} + \\ \sigma(r) \left\{ -\nabla \cdot \left(D(r) \nabla \left(\frac{\beta_1(r)}{\beta_0(r)}\Phi_1(r) + \frac{\beta_2(r)}{\beta_0(r)}\Phi_2(r) \right) \right) + \mu_a(r) \left(\frac{\beta_1(r)}{\beta_0(r)}\Phi_1(r) + \frac{\beta_2(r)}{\beta_0(r)}\Phi_2(r) \right) \right\} \\ (1 - \sigma(r)) \left\{ -\nabla \cdot \frac{1}{7\mu_{a3}(r)} \nabla \Phi_2(r) - \frac{2}{3}\mu_a(r)\Phi_1(r) + \left(\frac{4}{9}\mu_a(r) + \frac{5}{9}\mu_{a2}(r) \right) \Phi_2(r) \right\} \end{array} \right\} r \in \Omega, \quad (8)$$

$= S(r)$

$= -\frac{2}{3}(1 - \sigma(r))S(r)$

where $\sigma(r)$ is the introduced indicator factor and is defined as:

$$\sigma(r) = \begin{cases} 1 & r \in \Omega_l \text{ or } \partial\Omega \subset \partial\Omega_l \\ 0 & r \in \Omega_h \text{ or } \partial\Omega \subset \partial\Omega_h \end{cases}, \quad (9)$$

where $\partial\Omega$ is the outer boundary of the living body. In mathematics, the computational complexity of equation (8) is almost the same as that of equation (2). However, the improvement on the computational efficiency can be achieved during the process of programming implementation, because much less computational amount of DE in assembling the system matrix of HSDE and a bit more zero-value elements of the system matrix of HSDE in the matrix inversion would reduce the computation time of equation (8).

The relevant measurements can be obtained from the exiting partial current at the outer boundary of the living body that has the following expression:

$$J(r) = (1 - \sigma(r))J_{SP3}(r) + \sigma(r)J_{DE}(r) \quad r \in \partial\Omega, \quad (10)$$

where $J(r)$ is the exiting partial current at the outer boundary $\partial\Omega$ of the living body. Substituting equations (3), (5) and (7) into equation (10), the exiting partial current can be rewritten as:

$$J(r) = \beta_1(r)\Phi_1(r) + \beta_2(r)\Phi_2(r) \quad r \in \partial\Omega. \quad (11)$$

For convenience, the established HSDE can be rewritten as the following concise form:

$$-\nabla \cdot C_{k,\nabla\Phi_1}(r) \nabla \Phi_1(r) - \nabla \cdot C_{k,\nabla\Phi_2}(r) \nabla \Phi_2(r) + C_{k,\Phi_1}(r)\Phi_1(r) + C_{k,\Phi_2}(r)\Phi_2(r) = C_{k,S}(r)S(r) \quad r \in \Omega, \quad (12)$$

where the concrete forms of $C_{k,\nabla\Phi_1}(r)$, $C_{k,\nabla\Phi_2}(r)$, $C_{k,\Phi_1}(r)$, $C_{k,\Phi_2}(r)$, and $C_{k,S}(r)$ ($k = 1, 2$) are listed in the appendix. Equation (12) together with boundary condition equation (11) is the developed HSDE model that would provide a perfect balance between accuracy and computation time.

2.2. Finite element discretization of the HSDE model

Using the Gauss divergence theorem, the governing equation of HSDE, equations (11) and (12) can be equivalently deduced to the following weak form:

$$\int_{\Omega} \left\{ C_{k,\nabla\Phi_1}(r) (\nabla \Phi_1(r)) \cdot (\nabla \psi(r)) + C_{k,\nabla\Phi_2}(r) (\nabla \Phi_2(r)) \cdot (\nabla \psi(r)) + C_{k,\Phi_1}(r) \Phi_1(r) \psi(r) + C_{k,\Phi_2}(r) \Phi_2(r) \psi(r) \right\} dr + \int_{\partial\Omega} (\beta_1(r) \Phi_1(r) \psi(r) + \beta_2(r) \Phi_2(r) \psi(r)) dr = \int_{\Omega} C_{k,S}(r) S(r) \psi(r) dr. \quad (13)$$

Following the standard finite element method, the composite moments $\Phi_k(r)$ ($k = 1, 2$) and the light source $S(r)$ in equation (13) can be approximated with piecewise polynomial bases:

$$\begin{aligned} \Phi_k(r) &= \sum_{i=1}^{N_i} \phi_{k,i} \varphi_i(r) \\ S(r) &= \sum_{i=1}^{N_i} s_i \varphi_i(r) \end{aligned} \quad (14)$$

where $\phi_{k,i}$ is the nodal value of $\Phi_k(r)$ ($k = 1, 2$) on the i th node; s_i is the nodal value of $S(r)$; $\varphi_i(r)$ is the basis function; and N_i is the total number of discretized nodes.

By substituting equation (14) into equation (13), the following matrix equation can be obtained:

$$\begin{bmatrix} M_{11} & M_{12} \\ M_{21} & M_{22} \end{bmatrix} \begin{Bmatrix} \Phi_1 \\ \Phi_2 \end{Bmatrix} = [M] \begin{Bmatrix} \Phi_1 \\ \Phi_2 \end{Bmatrix} = \begin{bmatrix} F_{11} & 0 \\ 0 & F_{22} \end{bmatrix} \begin{Bmatrix} S \\ S \end{Bmatrix}, \quad (15)$$

where relevant components in the block matrices are detailed as:

$$\begin{cases} M_{11,ij} = \int_{\Omega} \left(C_{1,\nabla\Phi_1}(r) \nabla \varphi_i(r) \nabla \varphi_j(r) + C_{1,\Phi_1}(r) \varphi_i(r) \varphi_j(r) \right) dr + \int_{\partial\Omega} \beta_1(r) \varphi_i(r) \varphi_j(r) dr \\ M_{12,ij} = \int_{\Omega} \left(C_{1,\nabla\Phi_2}(r) \nabla \varphi_i(r) \nabla \varphi_j(r) + C_{1,\Phi_2}(r) \varphi_i(r) \varphi_j(r) \right) dr + \int_{\partial\Omega} \beta_2(r) \varphi_i(r) \varphi_j(r) dr \\ M_{21,ij} = \int_{\Omega} \left(C_{2,\nabla\Phi_1}(r) \nabla \varphi_i(r) \nabla \varphi_j(r) + C_{2,\Phi_1}(r) \varphi_i(r) \varphi_j(r) \right) dr + \int_{\partial\Omega} \beta_1(r) \varphi_i(r) \varphi_j(r) dr \\ M_{22,ij} = \int_{\Omega} \left(C_{2,\nabla\Phi_2}(r) \nabla \varphi_i(r) \nabla \varphi_j(r) + C_{2,\Phi_2}(r) \varphi_i(r) \varphi_j(r) \right) dr + \int_{\partial\Omega} \beta_2(r) \varphi_i(r) \varphi_j(r) dr \\ F_{11,ij} = \int_{\Omega} C_{1,S}(r) \varphi_i(r) \varphi_j(r) dr \\ F_{22,ij} = \int_{\Omega} C_{2,S}(r) \varphi_i(r) \varphi_j(r) dr \end{cases}$$

Computing the Moor–Penrose inverse of M and multiplying it on both sides of equation (15), we have:

$$\begin{aligned} \begin{Bmatrix} \Phi_1 \\ \Phi_2 \end{Bmatrix} &= [M^+] \begin{bmatrix} F_{11} & 0 \\ 0 & F_{22} \end{bmatrix} \begin{Bmatrix} S \\ S \end{Bmatrix} \\ &= \begin{bmatrix} M_{11}^+ & M_{12}^+ \\ M_{21}^+ & M_{22}^+ \end{bmatrix} \begin{bmatrix} F_{11} & 0 \\ 0 & F_{22} \end{bmatrix} \begin{Bmatrix} S \\ S \end{Bmatrix}. \end{aligned} \quad (16)$$

Then, Φ_k ($k = 1, 2$) can be represented by the block matrices:

$$\begin{cases} \Phi_1 = (M_{11}^+ F_{11} + M_{12}^+ F_{22})S \\ \Phi_2 = (M_{12}^+ F_{11} + M_{22}^+ F_{22})S \end{cases} \quad (17)$$

Only retaining the elements in the matrices M_{pq}^+ ($p, q = 1, 2$) and F_{pp} ($p = 1, 2$) that correspond to the measurable boundary in the exiting partial current equation, the linear relationship between the unknown distribution of the light source and the exiting partial current on the outer boundary is established as:

$$\begin{aligned} J &= (\beta_1(M_{11}^+ F_{11} + M_{12}^+ F_{22}) + \beta_2(r)(M_{21}^+ F_{11} + M_{22}^+ F_{22}))S \\ &= AS. \end{aligned} \quad (18)$$

Using the HSDE model to describe light propagation both in the excitation and emission process of FMT, the forward model for FMT reconstruction can be constructed. Similarly, the HSDE has the utility for bioluminescence tomography as well (Wang *et al* 2003, 2004, Gu *et al* 2004, Chaudhari *et al* 2005, Cong *et al* 2005, Lv *et al* 2006, Klose *et al* 2010).

3. Simulation studies

3.1. Accuracy demonstration of the HSDE model

The accuracy of the HSDE model was first demonstrated with regular geometries and digital mouse model based simulations. In comparison, the Monte Carlo method which was implemented in software for the molecular optical simulation environment (MOSE) (Ren *et al* 2013), was selected as the standard to validate the other numerical calculation models. To ensure accurate and reliable results of MOSE, simulations with 10^8 photons were performed for all of the comparisons. As for the references, the SP₃ and DE models were selected to illustrate the superiority of the HSDE model. An evaluation factor termed as the average relative error (ARE) was used to quantitatively describe the discrepancy between the numerical models and MOSE:

$$\text{ARE} = \frac{\sum_{i=1}^N (abs(f_i^{\text{std}} - f_i^{\text{cal}}) / \max(f_i^{\text{std}}))}{N}, \quad (19)$$

where f_i is the light partial current at the i th sample point; N is the total number of sample points; the superscript *std* denotes the light partial current obtained by MOSE and *cal* represents the light partial current calculated by the numerical models, including HSDE, SP₃ and DE. In the following comparisons, all of the calculations were conducted on a personal computer with a 3.1 GHz Inter(R) Core(TM) i5-2400 CPU and 8.00 GB RAM.

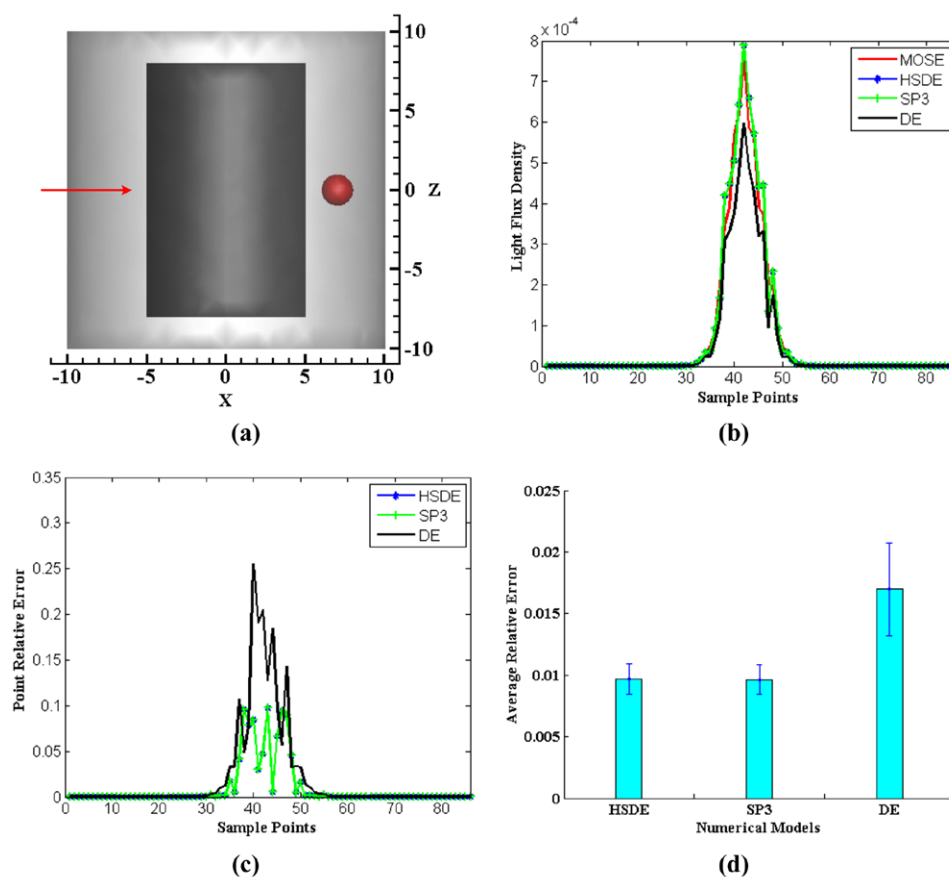


Figure 1. Comparison results of the simple regular geometry-based simulation. (a) Physical model used in the simulation; (b) One of the representative profiles of light flux density distribution at a height of $Z = 0$ mm; (c) Point relative error of (b); (d) Mean and variance of ARES for all five groups of simulations. In (b) and (c), the blue asterisks, green crosses and black lines show the calculation results of HSDE, SP₃, and DE respectively, and the red solid lines are on behalf of the simulation results of MOSE.

3.1.1. Simple regular geometry. First, the accuracy of the HSDE model was validated with the simple regular geometry based simulations. The geometry is comprised of two cylinders with their centers at the origin of the coordinates. The outer cylinder has a 10 mm radius and 20 mm height, and the inner one has a 5 mm radius and 16 mm height. A sphere with the radius of 1 mm is located at the position of (7,0,0) mm to mimic an internal light emission source. Figure 1(a) shows intuitive information of the geometry. For simplicity, the power of the light emission source was set to be 1 nW. To exclude the occasionality of the results, five groups of optical properties were utilized for the comparisons, as listed in table 1. To obtain smooth and reliable calculation results for the HSDE, SP₃ and DE models, the geometry was discretized into 11 190 nodes and 56 822 tetrahedrons. Comparisons between the calculation results of the numerical models (HSDE, SP₃, and DE models) and simulation results of MOSE are described in figure 1. Profiles of light flux density distribution at a height of $Z = 0$ mm (indicated by a red arrow in figure 1(a)) were sampled around the surface of the outer cylinder for all of the five groups of comparisons, and one of the representative profiles is shown in

Table 1. Optical properties used in simple regular geometry-based simulations.

Group		$\mu_a(\text{mm}^{-1})$	$\mu_s(\text{mm}^{-1})$	g	Classification
1	Outer	0.09	4.5	0.9	Other ^a
	Inner	0.02	3		High ^a
2	Outer	0.2	4		Other
	Inner	0.02	4		High
3	Outer	0.4	10		Other
	Inner	0.01	4		High
4	Outer	0.08	4		Other
	Inner	0.002	2		High
5	Outer	0.4	2		Other
	Inner	0.01	10		High

^a High: high scattering tissues; other: other tissues.

figure 1(b), where the blue asterisks, green crosses and black lines show the calculation results obtained by the HSDE, SP₃, and DE models respectively, and the red solid lines are on behalf of the simulation results of MOSE. To more intuitively observe the discrepancy, the relative error at each sampled point was also calculated and plotted in figure 1(c). The mean and standard deviation of AREs for all five groups of simulations are shown in figure 1(d). From figure 1, the following conclusions can be addressed. First of all, almost the same accuracy is obtained for the HSDE and SP₃ models, with a roughly identical tendency as the result of MOSE. Secondly, HSDE exhibits a much better accuracy than the DE model. The maximum relative error at the sampled point is less than 0.1, which is much smaller than that of the DE model (with the value larger than 0.25). In terms of ARE, the mean value of AREs for all the five groups of simulations is less than 0.01, which is also better than that of the DE model (with the value of 0.017). In order to further observe how the HSDE model improves the accuracy of the DE one, we extracted two groups of observed points from the high scattering and other tissues respectively and calculated the relevant AREs regarding the results of SP₃ as the standard. Very similar means and standard deviations of AREs are obtained for the HSDE and DE models in the high scattering regions, with the values of 0.019 ± 0.008 and 0.029 ± 0.010 respectively. However, in the other tissues, the HSDE model performs better than the DE one, with the smaller ARE (0.011 ± 0.003 versus 0.068 ± 0.011). This reveals that the HSDE model improves the accuracy of DE one in the other tissues' region. All in all, the HSDE model exhibits almost the same accuracy as SP₃ and has a much better performance than DE when the low scattering or high absorption regions exist in a regular geometry.

3.1.2. Complicated regular geometry. Second, a complicated regular geometry was employed to perform the accuracy demonstration simulation. The geometry is comprised of five objects, with their geometrical parameters and optical properties shown in figure 2(a) and table 2. Similarly, a sphere with a radius of 1.5 mm is located at position of (6,6,0) mm to mimic an internal light emission source, and the power of the source was set to be 1 nW. In this simulation, this geometry was discretized into 61 326 tetrahedrons and 11 427 nodes. Similar to simple regular geometry based simulations, a profile of light flux density distribution at a height of $Z = 0$ mm (indicated by a red arrow in figure 2(a)) was extracted for displaying the comparisons, as shown in figure 2(b). In figure 2(b), the blue asterisk, green cross and black solid lines show the calculation results of the HSDE, SP₃, and DE models respectively, and the red solid lines are the simulation results of MOSE. The ARE between HSDE and MOSE is 0.6724%, which is almost the same as that between SP₃ and MOSE (0.6723%) and much smaller than

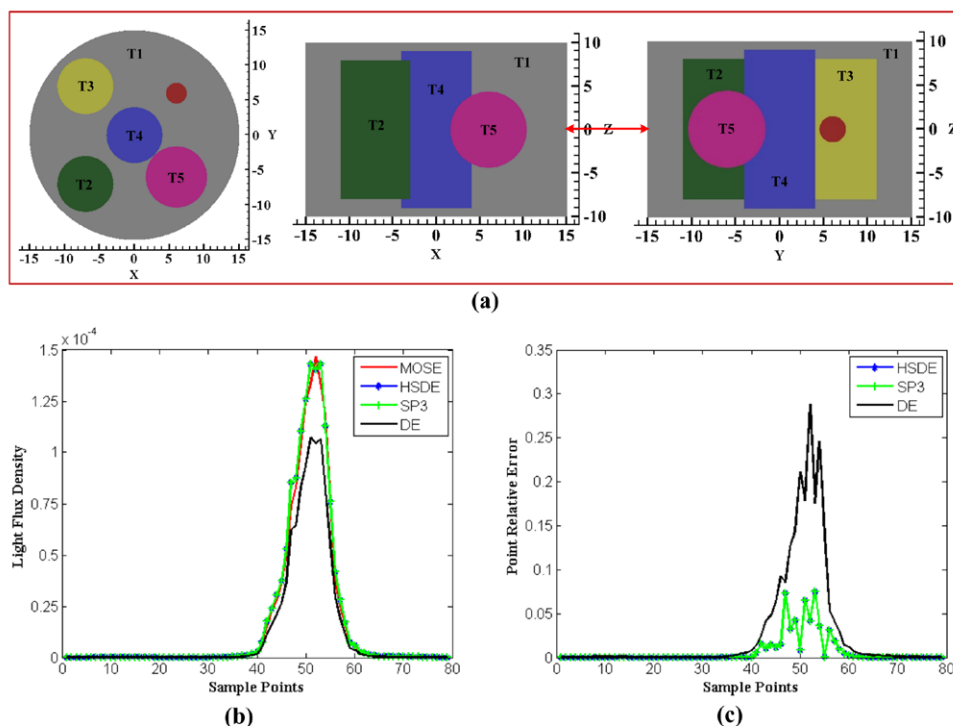


Figure 2. Comparison results of complicated regular geometry-based simulation. (a) Physical model used in the simulation; (b) Profiles of light flux density distribution at a height of $Z = 0$ mm; (c) Point relative error of (b). In (b) and (c), the blue asterisks, green crosses and black lines show the calculation results of HSDE, SP₃, and DE respectively, and the red solid lines are on behalf of the simulation results of MOSE.

the value between DE and MOSE (2.6755%). In addition, the point relative errors were also calculated on the sampled points and shown in figure 2(c). From figures 2(b) and (c), we find that the HSDE model exhibits almost exactly the same performance as the SP₃ model, both of which are consistent with MOSE and much better than the DE model. In figure 2(c), the maximum relative error for HSDE is about 7.5%, while that for DE is up to 28.8%. Similarly, the AREs in the high scattering tissues and the other tissues were also calculated respectively, which shows a better accuracy of the HSDE model than the DE one when they were compared with the SP₃ model. The AREs for the HSDE and DE are 0.019 and 0.03 in the high scattering tissue, and 0.01 and 0.044 in the other tissues. Results of this complicated regular geometry based simulation also reveal the superiority of the HSDE over the DE model in processing light propagation in the geometry with low scattering regions.

3.1.3. Digital mouse model. Third, a digital mouse model was used to verify the accuracy of the HSDE model in the irregular medium. The digital mouse model is comprised of several main organs, including adipose, heart, stomach, liver, kidneys, and lungs, which are extracted from the CT and cryosection data (Dogdas *et al* 2007), as presented in figure 3(a). The optical properties used in the simulation were calculated around the wavelength of 670 nm and are listed in table 3 (Alexandrakis *et al* 2005). A light emission source with a radius of 1 mm and power of 1 nW was positioned at (20,11,20) mm. In the following simulation, the digital

Table 2. Geometrical and optical parameters used in the complicated regular geometry-based simulation.

Tissue	Shape	$\mu_a(\text{mm}^{-1})$	$\mu_s(\text{mm}^{-1})$	g	Classification
T1	Cylinder	0.2	4	0.9	Other ^a
T2	Cylinder	0.01	4		High ^a
T3	Cylinder	0.04	6		High
T4	Cylinder	0.004	2		High
T5	Sphere	0.06	8		High

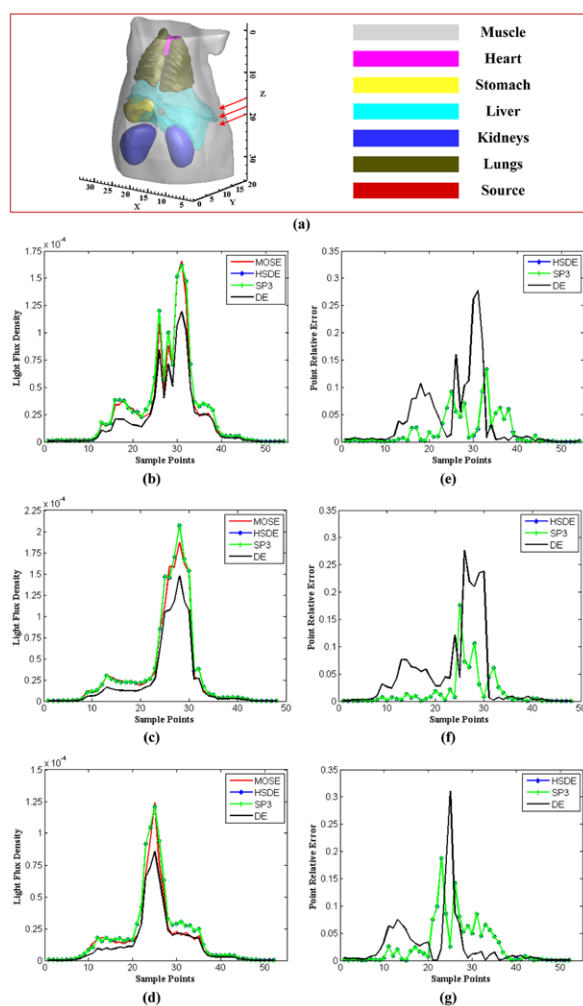
^a High: high scattering tissues; other: other tissues.**Figure 3.** Comparison results of the digital mouse model based simulation. (a) Physical model used in the simulation; (b)–(d) Profiles of light flux density distribution at height of $Z = 20, 18, 16$ mm respectively; (e)–(g) Point relative errors of (b)–(d) respectively. In (b)–(g) the blue asterisks, green crosses and black lines show the calculation results of HSDE, SP_3 , and DE respectively, and the red solid lines are on behalf of the simulation results of MOSE.

Table 3. Optical properties around the wavelength of 670 nm for the digital mouse model based simulation.

Tissue	Shape	$\mu_a(\text{mm}^{-1})$	$\mu'_s(\text{mm}^{-1})$	g	Classification
T1	Adipose	0.087	0.429	0.9	Other ^a
T2	Heart	0.059	0.643		High ^a
T3	Stomach	0.011	0.144		High
T4	Liver	0.352	0.678		Other
T5	Kidneys	0.066	1.609		High
T6	Lungs	0.196	3.623		High

^a High: high scattering tissues; other: other tissues.

mouse model is discretized into 93 112 tetrahedrons and 16 765 nodes. Three profiles of light flux density distribution at heights of $Z = 20, 18, 16$ mm (indicated by red arrows in figure 3(a)) were extracted and are shown in figures 3(b)–(d), where the blue asterisk, green cross and black solid lines are the calculation results of the HSDE, SP₃, and DE models respectively, and the red solid lines are the simulation results of MOSE. From figure 3(b)–(d), we can find that almost the same curvilinear tendency was obtained for the HSDE and SP₃ models, and both of them are in agreement with MOSE, which can also be observed from the values of ARE. The AREs between HSDE or SP₃ and MOSE are 2.0659% and 2.0641% respectively, which are smaller than that between DE and MOSE (with a value of 3.6383%). The point relative error at each sampled point also illustrates the superiority of HSDE over the DE model, as presented in figures 3(e)–(g). The largest point relative error for HSDE is smaller than 20%, while that for DE is larger than 25% and even up to 30%. Additionally, the ARE between the HSDE and SP₃ in the high scattering tissues is calculated as 0.0026, which is better than that between the DE and SP₃ models (0.034). Oppositely, in the other tissues, the accuracy of the HSDE is much better than that of the DE, with the rather smaller ARE (0.004 versus 0.07). Results of this simulation prove the accuracy of the HSDE model as well as reveal its superiority over the DE model in whole-body small animal imaging, for which the light propagation in the animal body with both the high scattering and other tissues should be processed better.

3.2. Efficiency investigation of the HSDE model

The accuracy of the HSDE model has been validated with regular geometries and digital mouse model based simulations in the previous section, whose results reveal the same accuracy as the SP₃ model and the superior accuracy over the DE model. Due to the low computation burden of DE, the HSDE model should take less time than the SP₃ one. Particularly, the time cost will become less and less with the increase in volume of the high scattering regions, in which DE will be executed. In this section, we investigated the execution efficiency of the HSDE model and how it will be affected by the ratio of the high scattering regions to the whole solving domain.

First, the computation times of the HSDE, SP₃, and DE models for the simulations presented in section 3.1 were recorded. To quantitatively observe the efficiency improvement of HSDE over SP₃, the following time saving ratio (TSR) is introduced and defined as:

$$(t_{\text{SP}_3} - t_{\text{HSDE}})/t_{\text{SP}_3},$$

where t_{SP_3} denotes the time cost of the SP₃ model, and t_{HSDE} is that of the HSDE one. Figures 4(a) and (b) present the computation time and relevant time saving ratio for the simple regular geometry based simulations. From figure 4(a) and (b), we find that the HSDE model

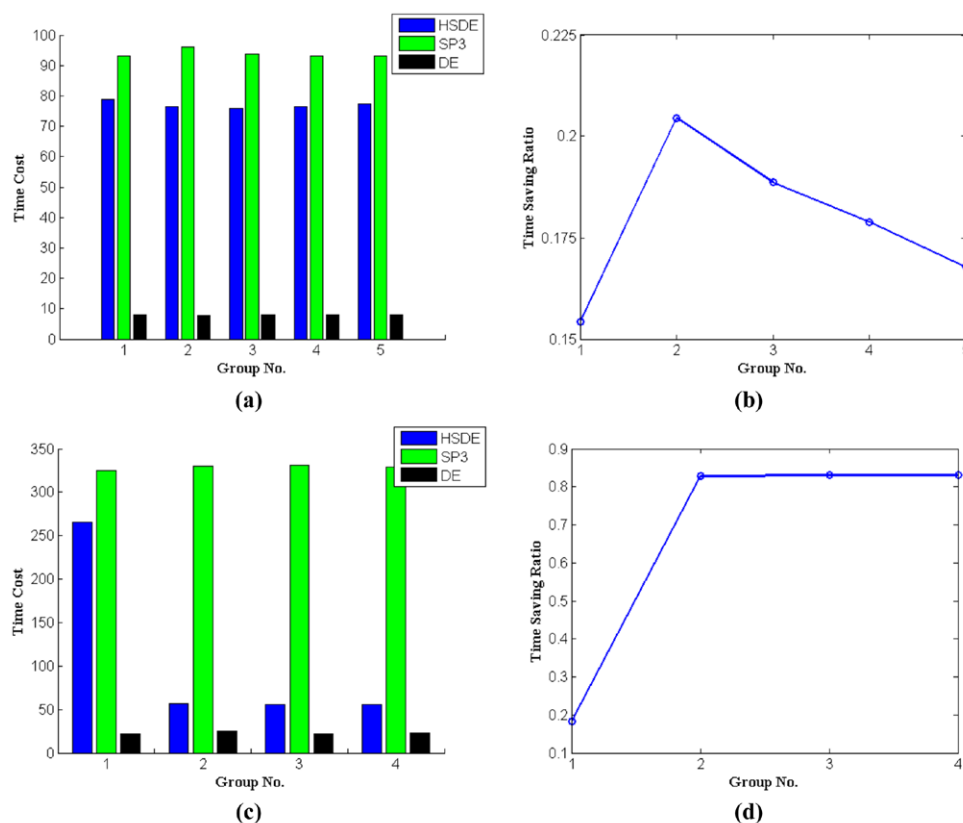


Figure 4. Computation times and relevant time saving ratios for the simulations presented in sections 3.1.1 and 3.1.3. (a) Computation times of the HSDE, SP₃, and DE models for the simple geometry used in section 3.1.1; (b) Time saving ratios corresponding to (a); (c) Computation times of the HSDE, SP₃, and DE models for the digital mouse model used in section 3.1.3; (d) Time saving ratios corresponding to (c). In the figures, the blue, green, and black bars are the time cost of HSDE, SP₃, and DE respectively. The computation time is in seconds.

indeed takes less time than the SP₃ one. Although the computation time is still much longer than the DE one, the efficiency is improved up to approximately 15–20% TSR compared with that of SP₃. For the complicated regular geometry based simulation, we also recorded the computation times for the HSDE, SP₃, and DE models. The time costs of the HSDE, SP₃, and DE models are 631.74, 871.28, and 30.07 s respectively. The computation efficiency is also improved with a TSR of 27.5%. For the digital mouse model based simulation, the time costs of the HSDE, SP₃, and DE models are recorded as 265.37, 324.87, and 22.35 s respectively, and the efficiency improvement is about 18.3%, which can be seen from the first group in figures 4(c) and (d). From these recorded computation times and improved efficiency, a very interesting phenomenon can be observed that all of the values of TSR are lower than 30%. By analyzing the experimental settings of the simulations, we find that all of the outer tissues of the geometries used in section 3.1 belong to the category of the other tissues which should be processed with the SP₃ equation and have more of a computation burden. If the outer tissue is changed to a high scattering one, the computational time should be less. To verify this hypothesis, we conducted another three groups of simulations using the digital mouse model.

Table 4. Optical properties around the wavelength of 670, 690, and 710 nm for the digital mouse model based simulation in the efficiency investigation. In units of mm^{-1} .

Tissue	Shape	No. 2: 670 nm		No. 3: 690 nm		No. 4: 710 nm		Classification
		μ_a	μ'_s	μ_a	μ'_s	μ_a	μ'_s	
T1	Muscle	0.004	2.013	0.003	1.982	0.003	1.952	High ^a
T2	Heart	0.059	0.643	0.044	0.616	0.033	0.591	High
T3	Stomach	0.011	0.144	0.009	1.746	0.007	1.698	High
T4	Liver	0.352	0.678	0.261	0.657	0.200	0.638	Other ^a
T5	Kidneys	0.066	1.609	0.049	1.539	0.038	1.474	High
T6	Lungs	0.196	3.623	0.145	3.567	0.111	3.513	High

^a High: high scattering tissues; other: the other tissues.

Table 5. Varying radii and the related volume ratios.

Group No.	Radius (mm)	V2/V1	V2/V (%)
1	5.2900	4/15	20.99
2	6.1721	6/15	28.57
3	6.8101	8/15	34.78
4	7.3030	10/15	40.00
5	7.6980	12/15	44.44

In the simulations, the outer tissue (T1) was changed from adipose to muscle, which is a high scattering tissue around the wavelength of 670, 690, and 710 nm. The detailed optical properties are listed in table 4. The computation times of the HSDE, SP₃, and DE models for the three groups of simulations are recorded and plotted in the 2nd–4th groups in figure 4(c). We find that great improvements on computational efficiency were obtained in all of the observed cases. The computation time of the HSDE model is only about two times longer than that of the DE one and much shorter than that of the SP₃, which can also be seen from the TSR plotting in figure 4(d). More than 80% of time can be saved by utilizing the HSDE model compared with the SP₃ one when the outer tissue is a high scattering tissue (the 2nd–4th groups in figure 4(d)). Thus, a conclusion can be made that the volume of the high scattering tissue will greatly affect the computational efficiency of the HSDE model, which has been validated with the following investigation simulations.

In the following investigation, simple regular geometry based simulations were conducted. The geometry is comprised of two cylinders with the centers at the origin of the coordinates. The outer cylinder has a dimension with a 10 mm radius and 24 mm height, and the inner one has an 18 mm height and a variable radius. With the changes in the radius of the inner cylinder, different values of the ratio between the volume of the high scattering region (simplified as V2) and that of the other region (simplified as V1) can be obtained, which also reflects the ratio between the volume of the high scattering region (V2) and that of the whole solving domain (simplified as V). The varying radii and relevant volume ratio are listed in table 5. The optical properties of the cylinders are specified as: for the outer cylinder, the absorption coefficient is 0.1 mm^{-1} and the reduced scattering coefficient is 0.2 mm^{-1} ; for the inner one, the absorption coefficient is 0.02 mm^{-1} and the reduced scattering coefficient is 0.4 mm^{-1} . To mimic the light emission source, a sphere with a radius of 1.5 mm is located at position of (−3, 0, 0) mm, with the source power of 1 nW.

Using HSDE, SP₃, DE, and MOSE, the light flux distribution on the geometry surface is obtained. Subsequently, AREs between the numerical models of HSDE, SP₃, DE and the

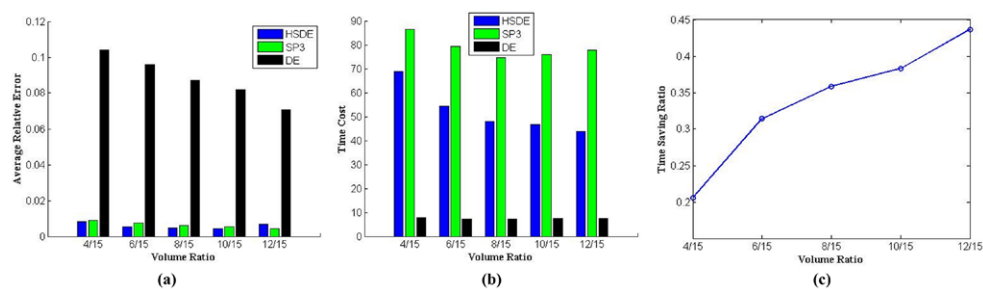


Figure 5. Results of the efficiency investigation simulation. (a) AREs between the numerical models (HSDE, SP₃, DE) and MOSE under different volume ratios; (b) Time cost for the numerical models of HSDE, SP₃, and DE under different volume ratios, presented in seconds; (c) Efficiency improvement of HSDE compared with SP₃ as the change in volume ratio. In the figures, the blue, green, and black bars are results of HSDE, SP₃, and DE respectively.

simulation one of MOSE are calculated. Figure 5(a) presents the AREs under the different volume ratios of the high scattering region to the whole solving domain. In the figures, the blue, green, and black bars are results of the HSDE, SP₃, and DE models respectively. We find that the accuracies of the HSDE and SP₃ models are almost the same as the stable AREs (smaller than 1%) with the change in volume ratio, which are much better than those of the DE model (greater than 7%). However, the ARE of the DE model becomes smaller with an increase in the ratio of the high scattering region. On the other hand, the time costs for executing the numerical models of HSDE, SP₃, and DE are recorded and plotted in figure 5(b). From figure 5(b), we can find that the time costs of the SP₃ and DE models stay relatively unchanged under different volume ratios. DE is the biggest timesaver model and SP₃ is the most time consuming one. In addition, HSDE exhibits good performance in efficiency, with less time cost than SP₃ under all of the observed volume ratios. Particularly, the efficiency of executing the HSDE model improves with less and less time as the volume of the high scattering region increases, which could also be observed from figure 5(c). Figure 5(c) presents efficiency improvement in the HSDE model compared with SP₃ as the volume ratio changes. From figure 5(c), we find that a 20–44% time-saver is obtained with the increase in the portion of the high scattering region. Results of this investigation reveal that the HSDE model integrates both a high-precision advantage of SP₃ and a low-computation-cost advantage of DE, so that it provides a perfect balance between accuracy and computation time.

4. Conclusion

In conclusion, the hybrid simplified spherical harmonics with diffusion equation (HSDE) based light transport model is proposed to describe fluorescence propagation in tissue for fluorescence tomography (FMT). The HSDE model can make full use of the advantages of SP_N and DE and abandon their disadvantages at the same time, so that it could provide a perfect balance between accuracy and computation time. Regular geometries and digital mouse model based simulations were conducted, whose results demonstrated the accuracy and efficiency of the HSDE model. Our future work will focus on the implementation and extensive applications of the HSDE based FMT reconstruction method, such as in longitudinal and quantitative monitoring of the development of *in situ* liver cancer as well as its drug therapy.

Acknowledgments

This work was supported by the Program of the National Basic Research and Development Program of China (973) under Grant No. 2011CB707702, the National Natural Science Foundation of China under Grant Nos. 81227901, 81230033, 81090272, 81101083, the Natural Science Basic Research Plan in Shaanxi Province of China under Grant Nos. 2015JQ6249, 2015JZ019, and the Fundamental Research Funds for the Central Universities.

Appendix

The concrete forms of coefficients $C_{k,\nabla\Phi_1}(r)$, $C_{k,\nabla\Phi_2}(r)$, $C_{k,\Phi_1}(r)$, $C_{k,\Phi_2}(r)$, and $C_{k,S}(r)$ ($k = 1, 2$) are listed as follows:

$$\begin{aligned}
 k = 1 \\
 C_{1,\nabla\Phi_1}(r) &= (1 - \sigma(r)) \frac{1}{3\mu_{a1}(r)} + \sigma(r) D(r) \frac{\beta_1(r)}{\beta_0(r)} \\
 C_{1,\nabla\Phi_2}(r) &= \sigma(r) D(r) \frac{\beta_2(r)}{\beta_0(r)} \\
 C_{1,\Phi_1}(r) &= (1 - \sigma(r)) \mu_a(r) + \sigma(r) \mu_a(r) \frac{\beta_1(r)}{\beta_0(r)} \\
 C_{1,\nabla\Phi_2}(r) &= (1 - \sigma(r)) \left(-\frac{2}{3} \mu_a(r) \right) + \sigma(r) \mu_a(r) \frac{\beta_2(r)}{\beta_0(r)} \\
 C_{1,S}(r) &= 1 \\
 \\
 k = 2 \\
 C_{2,\nabla\Phi_1}(r) &= 0 \\
 C_{2,\nabla\Phi_2}(r) &= (1 - \sigma(r)) \frac{1}{7\mu_{a3}(r)} \\
 C_{2,\Phi_1}(r) &= (1 - \sigma(r)) \left(-\frac{2}{3} \mu_a(r) \right) \\
 C_{2,\Phi_2}(r) &= (1 - \sigma(r)) \left(\frac{4}{9} \mu_a(r) + \frac{5}{9} \mu_{a2}(r) \right) \\
 C_{2,S}(r) &= -\frac{2}{3} (1 - \sigma(r))
 \end{aligned}$$

References

- Ale A *et al* 2012 FMT-XCT: *in vivo* animal studies with hybrid fluorescence molecular tomography-x-ray computed tomography *Nat. Methods* **9** 615–20
- Alexandrakis G, Rannou F R and Chatziioannou A F 2005 Tomographic bioluminescence imaging by use of a combined optical-PET (OPET) system: a computer simulation feasibility study *Phys. Med. Biol.* **50** 4225–41
- Arridge S R 1999 Optical tomography in medical imaging *Inverse Problems* **15** R41–93
- Chaudhari A *et al* 2005 Hyperspectral and multispectral bioluminescence optical tomography for small animal imaging *Phys. Med. Biol.* **50** 5421–41
- Chen J, Fang Q and Intes X 2012 Mesh-based Monte Carlo method in time-domain widefield fluorescence molecular tomography *J. Biomed. Opt.* **17** 106009

- Cong W *et al* 2005 Practical reconstruction method for bioluminescence tomography *Opt. Express* **13** 6756–71
- Darne C, Lu Y and Sevic-Muraca E 2014 Small animal fluorescence and bioluminescence tomography: a review of approaches, algorithm and technology update *Phys. Med. Biol.* **59** R1–64
- Davisa S *et al* 2013 Dynamic dual-tracer MRI-guided fluorescence tomography to quantify receptor density *in vivo* *Proc. Natl Acad. Sci. USA* **110** 9025–30
- Dehghani H, Delpy D T and Arridge S R 1999 Photon migration in non-scattering tissue and the effects on image reconstruction *Phys. Med. Biol.* **44** 2897–906
- Dogdas B *et al* 2007 Digimouse: a 3D whole body mouse atlas from CT and cryosection data *Phys. Med. Biol.* **52** 577–87
- Erickson S *et al* 2013 3D fluorescence tomography of human breast tissues *in vivo* using a hand-held optical imager *Phys. Med. Biol.* **58** 1563–79
- Firbank M *et al* 1996 An investigation of light transport through scattering bodies with non-scattering regions *Phys. Med. Biol.* **41** 767–83
- Fortin P *et al* 2012 Detection of brain tumors using fluorescence diffuse optical tomography and nanoparticles as contrast agents *J. Biomed. Opt.* **17** 126004
- Freiberger M, Egger H and Scharfetter H 2010 Nonlinear inversion schemes for fluorescence optical tomography *IEEE Trans. Biomed. Eng.* **57** 2723–9
- Gao H *et al* 2010 Fully linear reconstruction method for fluorescence yield and lifetime through inverse complex-source formulation: simulation studies *Opt. Lett.* **35** 1899–901
- Gibson A, Hebden J and Arridge S 2005 Recent advances in diffuse optical imaging *Phys. Med. Biol.* **50** R1–43
- Gorpas D *et al* 2010 A 3D finite elements approach for the coupled radiative transfer equation and diffusion approximation modeling in fluorescence imaging *J. Quant. Spectrosc. Radiat. Transfer* **111** 553–68
- Gorpas D *et al* 2012 Evaluation of a radiative transfer equation and diffusion approximation hybrid forward solver for fluorescence molecular imaging *J. Biomed. Opt.* **17** 126010
- Gu X *et al* 2004 3D bioluminescence tomography with model-based reconstruction *Opt. Express* **12** 3996–4000
- Han D *et al* 2010 Sparsity-promoting tomographic fluorescence imaging with simplified spherical harmonics approximation *IEEE Trans. Biomed. Eng.* **57** 2564–7
- Hyde D *et al* 2009 Hybrid FMT–CT imaging of amyloid- β plaques in a murine Alzheimer's disease model *NeuroImage* **44** 1304–11
- Hyde D *et al* 2010 Data specific spatially varying regularization for multimodal fluorescence molecular tomography *IEEE Trans. Med. Imag.* **29** 365–74
- Joshi A *et al* 2006 Fully adaptive FEM based fluorescence optical tomography from time-dependent measurements with area illumination and detection *Med. Phys.* **35** 1299–310
- Joshi A *et al* 2008 Radiative transport-based frequency-domain fluorescence tomography *Phys. Med. Biol.* **53** 2069–88
- Kim H *et al* 2010 PDE-constrained multispectral imaging of tissue chromophores with the equation of radiative transfer *Biomed. Opt. Express* **1** 812–24
- Klose A and Larsen E 2006 Light transport in biological tissue based on the simplified spherical harmonics equations *J. Comput. Phys.* **220** 441–70
- Klose A and Pöschinger T 2011 Excitation-resolved fluorescence tomography with simplified spherical harmonics equations *Phys. Med. Biol.* **56** 1443–69
- Klose A *et al* 2010 *In vivo* bioluminescence tomography with a blocking-off finite-difference SP3 method and MRI/CT coregistration *Med. Phys.* **37** 329–38
- Lambers F M *et al* 2012 Longitudinal *in vivo* imaging of bone formation and resorption using fluorescence molecular tomography *Bone* **52** 587–95
- Lehtikangas O *et al* 2013 Hybrid forward-peaked-scattering-diffusion approximation for light propagation in turbid media with low-scattering regions *J. Quant. Spectrosc. Radiat. Transfer* **116** 132–44
- Li M *et al* 2012 Reconstruction of fluorescence molecular tomography using a neighborhood regularization *IEEE Trans. Biomed. Eng.* **59** 1799–803
- Liu K *et al* 2010 Evaluation of the simplified spherical harmonics approximation in bioluminescence tomography through heterogeneous mouse models *Opt. Express* **18** 20988–1002
- Liu F *et al* 2012a Monitoring of tumor response to cisplatin by subsurface fluorescence molecular tomography *J. Biomed. Opt.* **17** 040504

- Liu X *et al* 2012b 4D reconstruction for dynamic fluorescence diffuse optical tomography *IEEE Trans. Med. Imag.* **31** 2120–32
- Lu Y *et al* 2009 Spectrally resolved bioluminescence tomography with the third-order simplified spherical harmonics approximation *Phys. Med. Biol.* **54** 6477–93
- Lu Y *et al* 2013 *In vivo* imaging of orthotopic prostate cancer with far-red gene reporter fluorescence tomography and *in vivo* and *ex vivo* validation *J. Biomed. Opt.* **18** 101305
- Lv Y *et al* 2006 A multilevel adaptive finite element algorithm for bioluminescence tomography *Opt. Express* **14** 8211–23
- Mohajerani P *et al* 2014 Fluorescence-aided tomographic imaging of synovitis in the human finger *Radiology* **272** 865–74
- Nahrendorf M *et al* 2009 Hybrid *in vivo* FMT-CT imaging of protease activity in atherosclerosis with customized nanosensors *Arterioscler Thromb. Vasc. Biol.* **29** 1444–51
- Ntziachristos V *et al* 2002a Fluorescence molecular tomography resolves protease activity *in vivo* *Nat. Med.* **8** 757–60
- Ntziachristos V *et al* 2002b Visualization of antitumor treatment by means of fluorescence molecular tomography with an annexin V-Cy5.5 conjugate *Proc. Natl Acad. Sci. USA* **101** 12294–9
- Ntziachristos V *et al* 2005 Looking and listening to light: the evolution of whole-body photonic imaging *Nat. Biotechnol.* **23** 313–20
- Quan G *et al* 2011 Monte Carlo-based fluorescence molecular tomography reconstruction method accelerated by a cluster of graphic processing units *J. Biomed. Opt.* **16** 026018
- Ren S *et al* 2013 Molecular optical simulation environment (MOSE): a platform for the simulation of light propagation in turbid media *Plos One* **8** e61304
- Ripoll J and Nieto-Vesperinas M 1999a Index mismatch for diffuse photon density waves at both flat and rough diffuse-diffuse interfaces *J. Opt. Soc. Am. A* **16** 1947–57
- Ripoll J and Nieto-Vesperinas M 1999b Scattering integral equations for diffusive waves: detection of objects buried in diffusive media in the presence of rough interface *J. Opt. Soc. Am. A* **16** 1453–65
- Rudge T, Soloviev V and Arridge S 2010 Fast image reconstruction in fluorescence optical tomography using data compression *Opt. Lett.* **35** 763–5
- Soubret A, Ripoll J and Ntziachristos V 2005 Accuracy of fluorescent tomography in the presence of heterogeneities: study of the normalized born ratio *IEEE Trans. Med. Imag.* **24** 1377–86
- Stuker F, Ripoll J and Rudin M 2011 Fluorescence molecular tomography: principles and potential for pharmaceutical research *Pharmaceutics* **3** 229–74
- Tan Y and Jiang H 2008 DOT guided fluorescence molecular tomography of arbitrarily shaped objects *Med. Phys.* **35** 5703–7
- Tarvainen T *et al* 2005 Coupled radiative transfer equation and diffusion approximation model for photon migration in turbid medium *Phys. Med. Biol.* **50** 4913–30
- Wang D, Song X and Bai J 2007 Adaptive-mesh-based algorithm for fluorescence molecular tomography using an analytical solution *Opt. Express* **15** 9722–30
- Wang G *et al* 2003 Development of the first bioluminescence CT scanner *Radiology* **229** 566
- Wang G *et al* 2004 Uniqueness theorems in bioluminescence tomography *Med. Phys.* **31** 2289–99
- Wang D *et al* 2009 A novel finite-element-based algorithm for fluorescence molecular tomography of heterogeneous media *IEEE Trans. Inf. Technol. Biomed.* **13** 766–73
- Wu B and Gayen S 2014 Fluorescence tomography of targets in a turbid medium using non-negative matrix factorization *Phys. Rev. E* **89** 042708
- Yang D *et al* 2013 Light transport in turbid media with non-scattering, low-scattering and high absorption heterogeneities based on hybrid simplified spherical harmonics with radiosity model *Biomed. Opt. Express* **4** 2209–23
- Yang D *et al* 2015 Performance investigation of SP3 and diffusion approximation for 3D whole-body optical imaging of small animals *Med. Biol. Eng. Comput.* in preparation (doi:10.1007/s11517-015-1293-8)
- Yi H *et al* 2013 Reconstruction algorithms based on l1-norm and l2-norm for two imaging models of fluorescence molecular tomography: a comparative study *J. Biomed. Opt.* **18** 056013
- Zacharakis G *et al* 2005 Volumetric tomography of fluorescent proteins through small animals *in vivo* *Proc. Natl Acad. Sci. USA* **102** 18252–7
- Zhang W *et al* 2013 Combined hemoglobin and fluorescence diffuse optical tomography for breast tumor diagnosis: a pilot study on time-domain methodology *Biomed. Opt. Express* **4** 331–48
- Zhang G *et al* 2014 A direct method with structural priors for imaging pharmacokinetic parameters in dynamic fluorescence molecular tomography *IEEE Trans. Biomed. Eng.* **61** 986–90
- Zhu Q *et al* 2011 A 3D finite element model and image reconstruction algorithm for time-domain fluorescence imaging in highly scattering media *Phys. Med. Biol.* **56** 7419–34